Optimization of Naphthol Green B adsorption and degradation by nZVI/CS/APT using Plackett–Burman designs and response surface methodology

Yajuan Zhang, Hui Xu*, Lei Tian, Minzhang Chen, Xu Dong Jiang, Guojun Gou, Yong Chen*

College of Petrochemical Technology, Lanzhou University of Technology, Lanzhou, China, Tel. +86 13639317927/+86 931 7823115; emails: xuhui@lut.cn (H. Xu), chenylut@126.com (Y. Chen), 1799797925@qq.com (Y. Zhang), 2528989045@qq.com (L. Tian), 1377380676@qq.com (M. Chen), 1020990948@qq.com (X.D. Jiang), 570121265@qq.com (G. Gou)

ABSTRACT

In this study, a novel nanoscale zero-valent iron/chitosan/attapulgite (nZVI/CS/APT) composite was successfully prepared and was employed to remove Naphthol Green B (NGB) from water. Compared to the individual components, the removal performance of the nZVI/CS/APT composite was observed to be dramatically improved. Further, the surface morphology of the composite was characterized, and the possible degradation mechanism was proposed. The results indicated that nanoscale zero-valent iron (nZVI) demonstrated high dispersity and reaction activity after supported by CS/APT. NGB was observed to be degraded into hypotoxic or non-toxic small molecules by nZVI/CS/APT. Further, the critical variables affecting the NGB removal efficiency were screened by the Plackett–Burman design. The interactive effects of the different factors and perfect removal conditions were further elucidated using the response surface methodology. The values of m_{Fe}/m_{CS-APT}, adsorbent dosage, and pH were determined to be the main influencing factors. The average removal efficiency of NGB was determined to be 97.34% (three replicated experiments), which was almost similar to 98.89% predicted by the model. These results demonstrated the reliability of the statistical optimization designs for predicting the efficient removal of NGB.

Keywords: Nanoscale zero valent iron; Naphthol green B; Optimization; Plackett–Burman; Response surface methodology

1. Introduction

With industrialization, water pollution has gradually increased to alarming levels. Specifically, the presence of heavy metal ions, pesticides, and dyes in water leads to an accelerated deterioration [1]. Among the various pollutants, organic dyes have attracted research attention due to their thermal, and light stability, oxidation, and water solubility. Naphthol green B (NGB), an anionic dye, is commonly employed for dyeing of wool, silk, and polyamide [2]. Due to its unique molecular structure, NGB is highly toxic and difficult to degrade. Moreover, the metallic elements infiltrate into the water along with dyes, thus, negatively impacting the environment and human health [3]. In recent years, adsorption, reduction, and degradation of pollutants the promising technique to remove contaminants.

Nanoscale zero-valent iron (nZVI), an environmental-friendly material, is commonly used as an adsorbent to eliminate the pollutants owing to its excellent mobility, high reactivity, low toxicity, and abundant surface-active sites [4,5]. Besides, nZVI possesses a core-shell structure comprising both metallic iron and iron oxides. The core provides the medium to degrade the contaminants, while the shell allows their effective adsorption [6]. However, the high surface energy, low chemical stability, and surface agglomeration of nZVI affect its practical applications [7–9]. In order

* Corresponding authors.

to achieve the effective application of nZVI, carriers have been developed to reinforce its adsorption and degradation performance. Attapulgite (APT), a hydrate magnesium-aluminum-silicate and non-metallic mineral possesses large specific surface area, rich functional groups, and rod-like morphology, which enables its use for pollutant removal [10]. Nevertheless, low adsorption capacity, long adsorption duration, and non-optimal reuse limit its applications. It has been reported that the use of a substrate with abundant active sites the adsorption efficiency of APT [11,12]. The chitosan (CS) substrate, obtained from natural chitin biopolymer, demonstrates optimal biocompatibility, biodegradability, and environmental-friendly character [13,14]. Further, CS has abundant amino (–NH$_2$) and imine (–NH) functional groups, which can be protonated under acidic conditions and subsequently adsorb the anionic dyes by electrostatic attraction [15]. In recent years, a few literature studies have focused on the modification of chitosan. For instance, Sun et al. [16] reported the synthesis of CS/APT, while Deng et al. [17] investigated the removal of tannic acid from aqueous solution by chitosan-coated attapulgite. Further, the development of chitosan-loaded nZVI and attapulgite-loaded nZVI has also been reported in the literature. Currently, the majority of the studies have reported the use of a single carrier to load nZVI, which makes it challenging to simultaneously achieve high specific surface area, optimal absorbability, and low cost due to the limitations of the material structure. A few studies have reported the use of CS/APT as a dispersant to load nZVI to achieve contaminant removal. The use of a composite carrier (CS/APT) to load nZVI can not only provide a high specific surface area, but also play an effective role in dispersion and stability. Moreover, the composite carrier combines the structural diversity, thus, allowing the diverse functional groups to adsorb a multitude of pollutants. In general, the conventional methodology of experimental design involves the variation of an operating variable, while the other variables are kept constant at a certain level. Such experimentation methodology requires many experiments, which are time-consuming and energy-intensive. In addition, this methodology is difficult to optimize and does not allow to study of the interaction effect [18]. The Plackett–Burman designs (PB) and response surface methodology (RSM) have emerged as effective statistical techniques for experimental design and parameter optimization [19]. The PB designs can rapidly and effectively identify the important factors affecting the process. On the other hand, RSM is used to evaluate the important factors along with analyzing the interactions among the response variables, thus, allowing the selection of the optimum reaction conditions [20]. Sreedharan et al. [21] used the PB experiments to determine the factors influencing the removal of MG, and RSM was employed to evaluate the interactions among the variables. In another study, Zhou et al. [22] investigated the *Candida tropicalis* Z-04 degradation process of phenol through the central composite design (CCD). An excellent correlation was observed between the predicted and experimental results, thus, confirming the validity and practicability of the statistical and optimization approach. Overall, the PB designs and RSM can not only optimize the contaminant removal condition but also effectively overcome the drawbacks of the traditional experimental method.

In this study, a novel nZVI/CS/APT composite was prepared by the liquid-phase reduction method. The developed composite was applied to remove the anionic dye NGB from aqueous solutions. The Plackett–Burman designs were used to screen the critical variables, whereas the response surface methodology was employed to optimize the experimental conditions, so as to achieve an enhanced degradation efficiency and significantly reduced process time and cost. The following have been achieved in this study: (1) a ternary composite was synthesized with the double carrier (CS/APT) supported nZVI, and the functional groups and surface morphology were analyzed by Fourier transform infrared (FTIR), X-ray diffraction (XRD), transmission electron microscopy (TEM), and X-ray photoelectron spectroscopy (XPS); (2) experiment was used to determine the influencing factors for NGB removal, PB experiment was used to select the main influencing factors, and RSM model was employed to optimize the experimental conditions; (3) the adsorption of NGB and its degradation mechanism by nZVI/CS/APT were analyzed by UV-vis and FTIR analyses.
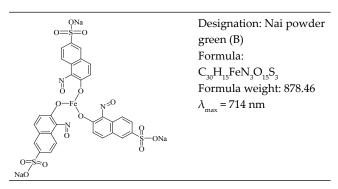
2. Experimental

2.1. Materials

Attapulgite (99%, APT) (JC-J503) was purchased from Jiangsu Xuyu Nanomaterial Science and Technology Co., Ltd., (China), analytical reagent grade ferrous sulfate heptahydrate (FeSO$_4$·7H$_2$O), sodium borohydride (NaBH$_4$) was purchased from Tianjin Kaixin Chemical Reagent Co., Ltd., China. Chitosan (CS) was purchased from Jinan Haidebei Marinev Biological Engineering Co., Ltd. Chemical structures of NGB (Chemical Reagent factory of Shanghai, China) are presented in Table 1. Hydrochloric acid (HCl), sodium hydroxide (NaOH), and they were used without any additional purification. All drugs were analytically pure and were not treated for directly using.

2.2. Materials preparation

The composite materials were synthesized by using the one-step method and Fe^0/CS-APT mass ratio of 1:1. Briefly, 0.25 g attapulgite and 0.25 g chitosan were added to 50 mL 0.05 mol L^{-1} HNO$_3$ solution, followed by ultrasonication for 30 min. Subsequently, the solution was heated to 60°C in a water bath, followed by stirring for

Table 1
General characteristic of the studied NGB

	Designation: Nai powder green (B)
	Formula: C$_{30}$H$_{15}$FeN$_3$O$_{15}$S$_3$
	Formula weight: 878.46
	λ_{max} = 714 nm

4 h. This acidic medium plays a dual function of purifying APT and protonating chitosan, thus, rendering chitosan and negatively charged APT to combine electrostatically. Afterwards, 1.2424 g FeSO$_4$·7H$_2$O was added at room temperature, and the contents were sonicated for 15 min to attain complete dissolution. Subsequently, 1.0133 g NaBH$_4$ (dissolved in 100 mL deionized water) was added dropwise under stirring and N$_2$ atmosphere. Finally, the composites with different m_{Fe}/m_{CS-APT} ratios (1:1, 5:2, and 4:1) were attained by filtering, washing, and drying the solids. The schematic of the synthesis CS/APT is shown in Fig. 1.

2.3. Characterization of methods

Fourier transforms infrared concerning composite materials was obtained employing FT-IR spectroscopy (NEXQS670, America) using KBr pellets. Morphology and structure of composite materials were observed by TEM (JEM-1200EX, and America). XRD patterns were collected on a X–ray diffract meter (XRD, D/MAX–2400X, Japan) using Cu Kα radiation (λ = 0.15406 Å) in a 2θ range of 10°–90° at room temperature. XPS data of nZVI/CS/APT composites were obtained using an ESCALAB 210 instrument. The GC/MS system consists of an Agilent 6890GC equipped with an Agilent 5973N mass selective detector (GC/MS) was used to detect the degradation products of NGB. Spectrophotometry was used for the measurement of the concentration of dyes in solution at specific adsorption wave on a 7230G spectrophotometer (Shanghai Precision Scientific Instrument Co., LTD., China). The N$_2$ adsorption–desorption, specific surface area, and pore size distribution of the sample were analyzed by American ASAP 2020 plus HD88 specific surface area and porosity analyzer, using the Barrett–Joyner–Halenda method, respectively. The pH measurements were conducted with a glass electrode (PHS-3D Model pH meter, China).

2.4. Adsorption analysis

The adsorption and NGB degradation process were performed as follows: 0.08 g nZVI/CS/APT was added into a conical flask containing 100 mL 50 mg L^{-1} NGB solution, and the reaction was performed for 40 min at 298 K. The solution pH was adjusted to the desired value by adding small amounts of HCl and NaOH. A small amount of solution was removed at regular intervals and filtered through 0.45 μm membranes to measure the residual concentration by using a UV spectrophotometer. The experiments were repeated at least thrice. The dye removal capacity and efficiency were calculated using Eqs. (1) and (2) as follows:

$$q = \frac{C_0 - C_t}{m} V \tag{1}$$

$$R = \frac{C_0 - C_t}{C_0} \times 100\% \tag{2}$$

where C_0 and C_t are the initial and equilibrium dye concentrations in solution (mg L^{-1}), V is the solution volume (L), and m is the mass of the adsorbent material (g).

The design-expert 10.0 software was employed to screen the influencing factors and optimize the experimental conditions.

3. Results and discussion

3.1. Material characterization

The FTIR characterization was performed to analyze the possible interaction between CS and APT, as shown in Fig. 2. The characteristic absorbance bands of APT at 3,555 and 3,421 cm^{-1}; 1,721; 1,515; and 1,115 cm^{-1} (Fig. 2a) were attributed to the vibrations of surface hydroxyl groups, mineral water, (Mg, Al)–Si–O and Si–O–Si, respectively [23]. The strong broad peak at 3,413 cm^{-1} was observed to overlap with the –O–H and –N–H stretching vibrations of CS (Fig. 2b), contributing to the hydrogen bond interaction between CS and APT. Further, the peaks at 2,916 and 2,850 cm^{-1} could be assigned to the –C–H stretching vibrations of the methylene and methyl groups, respectively. The stretching vibration band at 1,662 cm^{-1} was assigned to the amino group of CS [14]. Moreover, the characteristic adsorption band in the range 1,515–1,115 cm^{-1} represented the ether bond in CS [1]. For the CS/APT loaded nZVI (Fig. 2c), the characteristic peaks of CS and APT were observed in the composite materials. For the CS/APT loaded nZVI (Fig. 2c), the characteristic peaks of CS and APT were observed in the composite materials. In addition, the adsorption peaks located at 1,662; 1,515; and 1,115 cm^{-1} appeared to be slightly red-shifted in the composite materials, moving to 1,633; 1,418; and 1,036 cm^{-1}, respectively, which was mainly caused by the amino protonation of CS in acidic medium. The weak peak at 870 cm^{-1} was attributed to Fe–O, indicating the oxidation of the material surface exposed to air [14].

The XRD analysis was performed to verify the presence of nZVI and observe the changes in the valence states of iron before and after the reaction, as shown in Fig. 3. The characteristic peak at 2θ = 44.6° was attributed to bare nZVI, which was consistent with the published literature [24]. Prior to the reaction, the peak observed

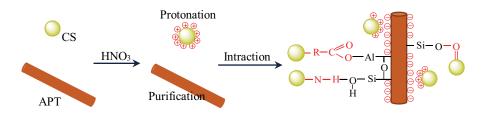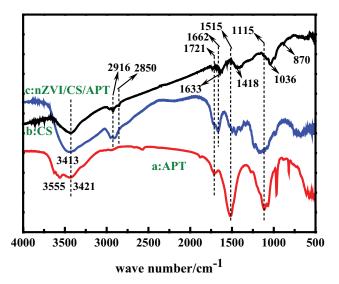Fig. 1. Schematic diagram of forms of materials based on CS and APT.

Fig. 2. FTIR spectra of (a) APT, (b) CS, and (c) nZVI/CS/APT.

Fig. 3. XRD patterns of nZVI, nZVI/CS/APT, and nZVI/CS/APT-NGB.

at 46.9° corresponded to Fe⁰, which was observed to shift probably due to the interaction between the precursor CS and APT. This indicated that nZVI was successfully loaded on the surface of CS/APT similar to the FTIR findings. Nevertheless, after interaction with NGB, the peak attributed to nZVI weakened and broadened, thus, leading to the formation of new peaks at 2θ = 21.5° (FeOOH) and 35.6° (Fe(II))/Fe(III) [25,26]. It indicated that nZVI was oxidized during the reaction, thus, confirming its important role in the NGB removal process.

The TEM investigation was performed to observe the dispersion of nZVI on the surface of CS/APT, as shown in
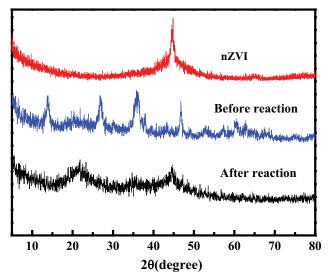
Fig. 4. The microstructure of the untreated APT appeared to be agglomerated and stacked mainly due to the electrostatic, hydrogen-bonding, and Van der Waals' forces among the rods (Fig. 4a) [23]. Chitosan was observed to be agglomerated due to the intra-molecular hydrogen bonding (Fig. 4b). Further, the nZVI particles were noted to be spherical and formed aggregated chain structures due to their magnetic properties (Fig. 4c) [13]. Compared with the individual materials, nZVI exhibited a uniform distribution after loading on CS/APT (Fig. 3d). It indicated that CS/APT enhanced the stability and potential reactivity of nZVI.
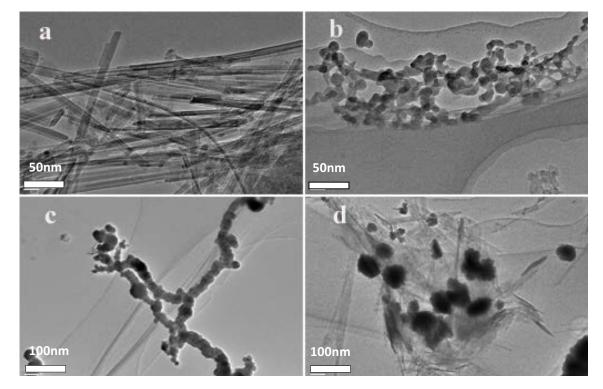

Fig. 4. TEM images of (a) APT, (b) CS, (c) fresh nZVI, and (d) nZVI/CS/APT.

In order to further confirm the outstanding dispersion of nZVI on CS/APT, the N₂ adsorption–desorption isotherms were measured, and the results are presented in Table 2. The shape of the adsorption–desorption isotherm did not exhibit any significant change, indicating that the composites with individual components maintained their complete framework. The S_{BET} value of nZVI and dispersant CS/APT were determined to be 17.51 and 19.90 m² g⁻¹. On the other hand, the S_{BET} value of nZVI/CS/APT reached up to 114.39 m² g⁻¹. It exhibited an almost seven-fold increment as compared to nZVI, signifying the suitability of CS/APT as a carrier to disperse nZVI. Simultaneously, the pore volume of nZVI/CS/APT (0.319 m³ g⁻¹) was noted to be superior to nZVI (0.024 m³ g⁻¹). The overall surface characteristics of nZVI/CS/APT demonstrated that CS/APT effectively prevented the reunion of nZVI, thus, enhancing the NGB removal efficiency.

The XRD analysis exhibited the changes in the valence state of nZVI before and after the reaction. The corresponding changes in the chemical composition of the composite surface were analyzed by XPS. Prior to the reaction (Fig. 5a), the peaks at 709.8 and 719.2 eV corresponded to Fe⁰ (2p3/2) and Fe⁰ (2p1/2), confirming that nZVI was successfully loaded on the CS/APT surface [27]. Furthermore, the peaks at 711.3, 712.8, and 724.8 eV, respectively, correspond to Fe₂O₃ (2p3/2), FeOOH (2p3/2), and Fe (III) (2p1/2) [28], which demonstrated a thin oxide layer covering the surface of nZVI, as also observed in the TEM images. After the reaction (Fig. 5b), the peaks at 709.8 and 719.2 eV were observed to disappear or weaken significantly, indicating the participation of nZVI in the NGB removal process.

3.2. Effect of different constituents on NGB removal

The rate of removal of NGB as a function of the different constituent materials is shown in Fig. 6. As APT, CS, and CS/APT inhibited the adsorption of anion dye owing to the negatively charged surfaces, the NGB removal rates of 9.9%, 50.1%, and 56.6% were observed after 40 min [29,30]. The removal rate of pure nZVI was observed to be 77.7%, which indicated that the agglomeration of nZVI reduced the number of effective adsorption active sites, as

Table 2
BET data of the materials

Materials	S_{BET} (m² g⁻¹)	V (m³ g⁻¹)	D (nm)
nZVI	17.51	0.024	10.39
CS/APT	19.90	0.044	11.68
nZVI/CS/APT (4:1)	114.39	0.319	12.40

also confirmed by TEM and BET. However, the removal rate of nZVI was much higher than CS/APT, confirming that nZVI played an important role in the dye removal process. In contrast, the removal rates in the case of nZVI/CS/APT (4:1, 5:2, and 1:1) were 95.5%, 91.3%, and 88.2%, respectively. Thus, the effectiveness of nZVI was significantly improved after supporting on CS/APT. Among the composites, the composite with m_{Fe}/m_{CS-APT} ratio of 4:1 exhibited the maximum removal efficiency.

3.3. Single-factor effect on NGB removal

3.3.1. Effect of initial NGB concentration

The NGB removal capacity of nZVI/CS/APT as a function of the NGB concentration has been presented in Fig. 7a. The removal efficiency of nZVI/CS/APT was observed to decrease on enhancing the NGB concentration. After 40 min, the removal rates were observed to be is 95.4%, 83.0%, and 79.5% for NGB concentrations of 50, 75, and 100 mg L⁻¹, respectively. The observed phenomenon indicated that nZVI/CS/APT could rapidly adsorb and degrade NGB at low concentrations. Thus, the maximum NGB removal efficiency was obtained for the dye concentration of 50 mg L⁻¹.

3.3.2. Effect of adsorbent dosage

The effect of the adsorbent amount (80–150 mg) on the removal rate has been presented in Fig. 7b. As the amount of adsorbent was increased from 80 to 100 mg and 150 mg, the removal rates were observed to increase from 95.4% to 96.0% and 98.5%, respectively. Correspondingly, the
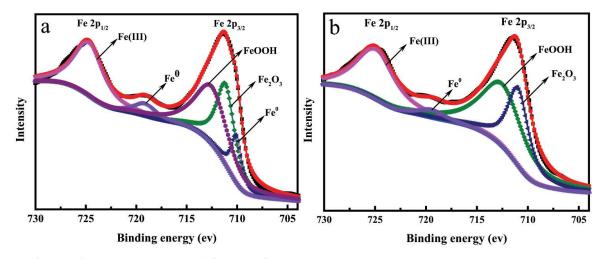

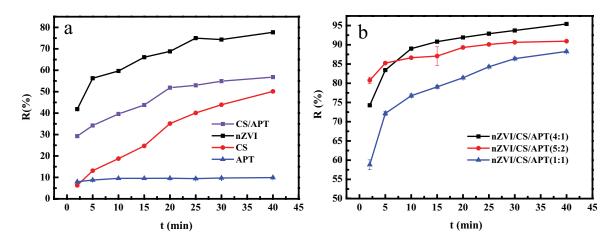Fig. 5. XPS of Fe 2p of nZVI/CS/APT reaction before and after with NGB.

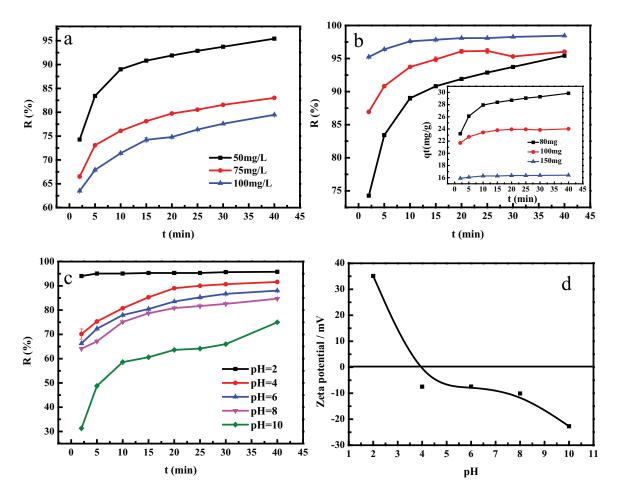Fig. 6. Different materials effect on removal of NGB effects.

Fig. 7. Effect removal efficiency of NGB (a) dye solution concentration, (b) amount of adsorbent, (c) pH, and (d) zeta potential of nZVI/CS/APT as a function of solution pH.

adsorption capacities were determined to be 29.9, 24.0, and 16.4 mg g^{-1}. Thus, the removal efficiency was gradually increased with the adsorbent dosage. The observed phenomenon could be attributed to the fact that the effective active sites increased with the adsorbent amount, which improved the ability of the composite to capture NGB. However, the significant agglomeration of nZVI/CS/APT on increasing the adsorbent content led to a reduction in adsorption capacity.

3.3.3. Effect of pH

The adsorption and degradation of NGB by nZVI/CS/APT was studied in the pH range 2–10, using 50 mg L^{-1}

dye concentration and 80 mg adsorbent. The corresponding NGB removal efficiency is presented in Fig. 7c. At the pH values of 2, 4, and 6, the removal efficiency was determined to be 95.7%, 91.6%, and 88.4%, respectively. As the pH value was further increased to 8 and 10, the removal rate after reaction 40 min was 84.8% and 75%, respectively. Therefore, it could be concluded that the acidic conditions were more conducive for NGB removal. For pH > 7, the combination OH⁻ and Fe⁰ formed a hydroxide coating on the adsorbent surface, which hindered the contact between nZVI/CS/APT and the dye molecules. At pH = 2, the abundant amino (–NH_2) and imine (–NH) groups on the adsorbent surface protonated to form –NH^{3+} and –NH^{2+}, making the adsorbent positively charged [31]. The observed phenomenon was also confirmed by the variation in the zeta potential (Fig. 7d). Consequently, the pH_{zpc} value of 3.9 was determined for nZVI/CS/APT. It indicated that the surface had a net zero charge at pH = 3.9, while the net positive and negative charges existed below and above this value. For pH < 3.9, the NGB removal resulted due to the electrostatic attraction, adsorption, and degradation. On the other hand, for pH > 3.9, the electrostatic effect disappeared, and the removal of NGB was mainly driven by adsorption and degradation. The observed findings indicated that an electrostatic interaction existed between the adsorbent and dye molecules under acidic conditions. The acidic solution has also been reported to promote the corrosion of nZVI, which enhances the active sites on the adsorbent surface for effective NGB removal [31].

3.4. Plackett–Burma experimental design

3.4.1. Experimental design

The PB designs are the effective screening method to identify the significant influencing factors among the variables [32]. In this study, the PB designs were used to filter the factors influencing the adsorption and degradation of NGB. Based on the literature studies on dye removal [33–36], the initial pollutant concentration adsorbent dosage, pH, and reaction time were chosen as the independent variables. In addition, the nZVI content and particle size were also included as variables. Table 3 lists the five variables and their corresponding levels, whereas the experimental findings are presented in Table 4.

3.4.2. Statistical analysis

The design-expert 10.0 software was used for the multivariate regression analysis of the experimental data, and the findings are presented in Table 5. The *P*-value for the regression model was determined to be 0.0077 (<0.05), indicating that the mode was significant and capable of accurately describing the relationship between the influencing factors and NGB removal rate. The influence of pH (*A*), $M_{adsorbent}$ (*B*), and $m_{Fe}/m_{CS\text{-}APT}$ (*C*) on the NGB removal efficiency was observed to follow the sequence: *A* (*P* = 0.0023) > *C* (*P* = 0.0330) > *B* (*P* = 0.0181). Meanwhile, the regression coefficient of pH (*A*) was negative, which signified a reduction in the NGB removal efficiency on enhancing the pH value. In contrast, the regression

Table 3
Levels of the variables tested in Plackett–Burman design

Factors	Significance of the factor	Unit	Low level (−1)	High level (+1)
A	pH	–	2	10
B	$M_{adsorbent}$	mg	80	150
C	$m_{Fe}/m_{CS\text{-}APT}$	g	1:1	4:1
D	Time	min	30	40
E	C_0	mg L⁻¹	50	100

Table 4
Plackett–Burman experimental combination and results (coded value)

Run order	pH	C_0	$M_{adsorbent}$	Time	$m_{Fe}/m_{CS\text{-}APT}$	R_{NGB} (%)
1	−1	−1	−1	1	−1	88.21
2	−1	1	−1	1	1	97.71
3	1	−1	1	1	−1	63.67
4	1	1	−1	−1	−1	33.66
5	1	1	1	−1	−1	53.50
6	−1	1	1	1	−1	80.56
7	−1	−1	−1	−1	−1	59.30
8	−1	−1	1	−1	1	96.03
9	1	−1	−1	−1	1	60.82
10	1	1	−1	1	1	47.23
11	−1	1	1	−1	1	99.62
12	1	−1	1	1	1	88.45

coefficients of $M_{adsorbent}$ (*B*) and $m_{Fe}/m_{CS\text{-}APT}$ (*C*) were positive, demonstrating the high NGB removal rates on enhancing the adsorbent amount and Fe⁰/CS-APT mass ratio. The multivariate linear equation could be written as Eq. (3):

$$R = 72.4 - 14.51A - 3.68B + 7.91C + 5.24D + 9.25E \qquad (3)$$

where *R* is the NGB removal rate, whereas the influencing factors *A*, *B*, *C*, *D*, and *E* represent pH, adsorbent dosage (mg), Fe⁰/CS-APT mass ratio (g), initial concentration (mg L⁻¹), and reaction time (min), respectively.

3.5. Response surface methodology to optimize the influencing factors

3.5.1. Experimental design and response results

The Box–Behnken design (BBD) (design-expert 10.0 software) was used to optimize the experimental conditions for NGB adsorption and degradation. The pH, adsorbent dosage, and Fe⁰/CS-APT mass ratio were used as the main influencing factors, whereas the NGB removal efficiency was employed as the response value. Table 6 presents the factorial design, whereas the findings from the 17 experiments suggested by the BBD model designs and values of the various factors in Table 6 are demonstrated in Table 7.

Table 5
Analysis of variance of nZVI/CS/APT adsorption NGB removal rate regression equation

Source	Sum of squares	df	Mean square	Coefficient	F	P > F*	Significance
Model	4,796.04	5	959.21	72.40	9.71	0.0077	Significant
A-pH	1,026.19	1	1,026.19	−14.51	25.58	0.0023	1
B-$M_{adsorbent}$	750.64	1	750.64	7.91	7.60	0.0330	3
C-$m_{Fe}/m_{CS\text{-}APT}$	162.89	1	162.89	9.25	10.39	0.0181	2
D-time	329.80	1	329.80	5.24	3.34	0.1174	
E-C_0	2,526.52	1	2,526.52	−3.68	1.65	0.2464	
Residual	592.68	6	98.78				
Cor total	5,388.72	11					

*$P > F$ is the significance level, and a value less than 0.05 are considered as significant.

Table 6
Assigned concentrations of variables at different levels

	Coded value	A-pH	B-$M_{adsorbent}$ (mg)	C-$m_{Fe}/m_{CS\text{-}APT}$ (g)
	−1	2	80	1:1
Level	0	6	115	5:2
	1	10	150	4:1

3.5.2. Response surface methodology, regression equation, and model analysis

The obtained response data were fitted using the quadratic regression analysis, and the results of variance analysis performed by using design-expert 10.0 software are shown in Table 8. A quadratic equation was obtained with the NGB removal rate as the response value and pH (A), adsorbent dosage (B), and Fe⁰/CS-APT mass ratio (C) as the independent variables as:

$$R = 96.86 - 5.76A + 6.7B + 3.76C + 4.17AB - 4.95AC - 2.59BC - 9.14A^2 + 2.35B^2 - 5.53C^2 \tag{4}$$

As shown in Table 8, the model probability value of 0.0005 (<0.01) confirmed that the quadratic regression variance model was significant. Meanwhile, the lack of fit ($P = 0.0530$) was not significant (>0.05), indicating that model prediction was consistent with the experimental results. Further, the R^2 value of 0.9585 influencing factors of the model. Therefore, the model was confirmed to be useful to predict and analyze the optimal adsorption conditions for removing NGB from an aqueous solution.

3.5.3. Interactive effects of factors on the NGB removal rate

The response surface diagrams for pH, adsorbent dosage, and Fe⁰/CS-APT mass ratio are displayed in Fig. 8. Fig. 8a presents the effect of pH and adsorbent dosage on the NGB removal performance at a constant Fe⁰/CS-APT mass ratio. As observed, the removal rate was observed to increase initially, with a subsequent decrease, on increasing pH. Further, the removal efficiency increased with the adsorbent

Table 7
BBD experimental combination design scheme and results (coded value)

Test number	A-pH	B-$M_{adsorbent}$	C-$m_{Fe}/m_{CS\text{-}APT}$	R_{NGB} (%)
1	1	1	0	98.27
2	0	1	0	98.76
3	0	1	−1	98.52
4	−1	0	1	99.24
5	1	−1	0	73.42
6	−1	−1	0	89.85
7	0	−1	1	93.67
8	−1	0	−1	79.73
9	−1	1	0	98.03
10	0	0	0	99.06
11	0	0	0	97.18
12	0	0	0	96.94
13	0	0	0	95.12
14	1	0	1	74.39
15	1	0	−1	74.70
16	0	0	0	95.12
17	0	−1	−1	83.06

amount. Therefore, the pH and adsorbent dosage exhibited an antagonistic interaction.

Fig. 8b displays the effect of pH and Fe⁰/CS-APT mass ratio on the NGB removal performance at a constant adsorbent amount. The removal rate was observed to increase initially, with a subsequent decrease, on increasing pH and Fe⁰/CS-APT mass ratio, thus, indicating a synergistic interaction between pH and Fe⁰/CS-APT mass ratio. Similarly, the interaction between the adsorbent amount and Fe⁰/CS-APT mass ratio was observed to be non-significant Fig. 8c.

3.5.4. Model optimization and experimental verification

The NGB removal efficiency was determined to be 98.89% by BBD by using the following conditions: pH = 2, 80 mg adsorbent dosage m_{nZVI}:$m_{CS\text{-}APT}$ = 4:1, 50 mg L⁻¹ solution

Table 8
Analysis of variance of nZVI/CS/APT adsorption removal NGB

Source	Sum of squares	df	Mean square	*F*-value	*P*-value Prob > *F*
Model	1,445.60	9	160.62	17.98	0.0005 (significant)
A-pH	265.20	1	256.60	29.69	0.0010
B-M$_{adsorbent}$	358.80	1	358.80	40.17	0.0004
C-m$_{Fe}$/*m*$_{CS-APT}$	112.59	1	112.95	12.65	0.0093
AB	98.19	1	98.19	10.99	0.0270
AC	69.44	1	69.44	7.77	0.0128
BC	26.85	1	26.85	3.01	0.1256
A^2	351.58	1	351.58	39.36	0.0004
B^2	128.85	1	128.85	14.43	0.067
C^2	23.19	1	23.19	2.60	0.1511
Residual	62.52	7	8.93		
Lack of fit	51.68	3	17.23	6.35	0.0530 (not significant)
Pure error	10.85	4	2.71		
Cor total	1,508.13	16			

Fig. 8. Response surface graphs of pH value, adsorbent dosage, and Fe⁰/CS-APT mass ratio on NGB removal rate.

concentration, and 40 min reaction duration, and the result was shown in Table 9. Three parallel experiments were carried out using these conditions, and the actual mean NGB removal rate was observed to be 97.34%. The relative deviation between the predicted and experimental values was

1.59%, which confirmed that the model optimization was accurate and credible. Besides, Table 10 summarizes the removal rates of the various adsorbents reported in the literature for removing NGB. It is worth noting that the nZVI/CS/APT composite developed in this study exhibits higher

Table 9
Experimental verification of the optimal removal rate

Parameters	Expected values	Experiment 1	Experiment 2	Experiment 3	Mean value	Relative error
pH	2	2	2	2		
M (mg)	80	80	80	80		
m_{Fe}/m_{CS-APT} (g)	4:1	4:1	4:1	4:1		
R (%)	98.89	96.94	97.24	97.85	97.34	1.59%

Table 10
Adsorption capacities of various adsorbents for NGB

Dye	Adsorbent	R (%)	Adsorption time (min)	Literature
	nZVI/CS/APT	97.34	40	This paper
	Magnetic halloysite-iron oxide	94.89	40	[37]
	Kaolinite	95.50	60	[38]
NGB	Charcoal	94.92	60	[38]
	Tafla	87.58	60	[38]
	MHS	93.00	30	[39]

removal efficiency and shorter equilibrium time as compared to the majority of the earlier reported adsorbents. Therefore, the nZVI/CS/APT composites represent a promising class of materials for removing binary dyes from wastewater.

3.6. NGB removal and degradation mechanism

Fig. 9a presents the UV-vis spectra of the NGB degradation process by nZVI/CS/APT as a function of time (0–40 min). Prior to the reaction, the UV-vis spectrum demonstrated three distinct peaks at 298, 347, and 714 nm attributed to the benzene ring (and around conjugated bond), phenolic group (and around conjugated bond), and –NO of ligand, respectively [40]. The absorption peak at 714 nm was observed to weaken after carrying out the reaction for 2 min. After 5 min, the peak was noted to disappear completely, which indicated that the chromophoric group (–N=O) of NGB was decomposed.

Also, the solution color changed from dark green to pale yellow to colorless in the end. The possible degradation mechanism of NGB was as follows: initially, the iron-complexes were released in NGB. Subsequently, the sulfone group was removed, and the –N=O group opened under the redox effect of nZVI. Eventually, NGB was decomposed into the less-toxic or non-toxic small molecules, allowing the mineralization of dye and eliminating its harmful effect on the ecological environment.

Fig. 8b presents the FTIR spectra of NGB and nZVI/CS/APT after the reaction. The NGB spectrum exhibited the characteristic peak of Fe–O at 3,413 cm^{-1}. The characteristic peaks at 1,609; 1,300; and 1,121 cm^{-1} could be attributed to the vibrations of naphthalene, –N=O, and sulfonic groups (Fig. 9b) [41]. Compared with the FTIR spectrum of nZVI/CS/APT prior to the reaction (Fig. 4), new characteristic peaks corresponding to NGB appeared in the spectrum after the reaction (Fig. 9a). This indicated that NGB and its degraded
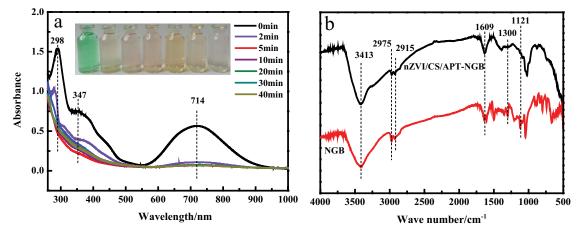

Fig. 9. UV-vis adsorption spectra of NGB at different reaction time (0–40 min) by nZVI/CSAPT (a) and the FITR of nZVI/CS/APT-NGB and NGB (b).

Table 11
Potential degradation products of NGB on nZVI/CS/APT

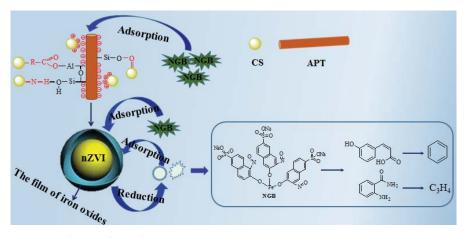| Products	Molecular formula	m/z	Relative intensity	Proposed structure
1	$C_{10}H_{10}O_7SFeNa$	354	[M–1]	
2	$C_{10}H_5O_7SFe$	323	[M+2]	
3	$C_{10}H_6O_2SN$	203	[M+1]	
4	$C_{10}H_{12}O_2N$	178	[M–1]	
5	$C_9H_8O_3$	161	[M+3]	
6	$C_8H_6O_3$	149	[M+1]	
7	$C_7H_8ON_2$	135	[M+1]	
8	C_7H_7N	103	[M+2]	
9	C_7H_8	91	[M+1]	
10	C_6H_6	77	[M+1]	
11	C_3H_5CN	65	[M+2]	$CH_2=CH–CH_2–C\equiv N$
12	C_2H_4CN	51	[M+2]	$CH_2=CH–C\equiv N$
13	C_3H_4	39	[M+1]	$CH_3–C\equiv CH$

Fig. 10. Potential degradation pathway of NGB by nZVI/CS/ATP.

intermediates were adsorbed on the surface of nZVI/ APT. As expected, the synergistic effect of nZVI and CS/ APT involved the adsorption of NGB on CS/APT and its degradation by nZVI.

The aliquots were subjected to the GC-MS analysis after a reaction duration of 40 min, and the potential degradation products of NGB are listed in Table 11. As nZVI/ CS/APT reacted with NGB, nZVI oxidized to Fe^{3+} and Fe^{2+} by losing electrons. These electrons enable NGB to release the composite iron to form a naphthalene hydroxyl compound, namely nitro-tetrahydronaphthol (m/z 178 [M–1]). 3-phenol-acrylic acid (m/z 161 [M+3]) and 2-amino-benzamide (m/z 135[M+1]) were also monitored in the NGB degradation products. Evidently, the chromophoric –N=O group was transformed into COOH and NH_2 [42]. At this stage, the chromophoric group of NGB disappeared, and the naphthalene ring was disconnected to reduce the toxicity of the naphthol compound [43]. Finally, NGB was degraded into benzene (m/z 77[M+1]) and alkynes (m/z 39[M+2]), realizing the cost-efficient degradation and toxicity reduction to provide the favorable basis for complete mineralization. The degradation process proposed in this study is also consistent with the literature studies [44]. Fig. 10 presents the proposed NGB degradation process.

4. Conclusion

In this study, NGB was effectively degraded into non-toxic small molecules by disconnecting N=O and naphthalene under the action of nZVI/CS/APT. The reactivity and dispersion of nZVI were observed to be immensely improved after loading nZVI on CS/APT. To achieve cost-efficient NGB removal, the statistical experimental designs (PB and RSM) were applied to optimize NGB degradation by nZVI/CS/APT. The PB designs screened the main influencing factors, whereas RSM effectively evaluated the interactive effects of the different factors, along with obtaining the optimum removal conditions. The model predicted the NGB removal rate to be maximum (97.34%) at the following conditions: $m_{Fe}/m_{CS\text{-}APT}$ mass ratio of 4:1, 75 mg adsorbent dosage and pH = 2. Further, the relative error between the experimental and predict values was only 1.59%. The value of the correlation coefficient (R^2) was determined to be 0.9585, which confirmed that the developed model could effectively predict and analyze the NGB removal. The optimal conditions obtained in this study lay the foundation for the use of nZVI/CS/APT for treating the organic dyes-containing effluents.

Acknowledgments

References

[1] C. Jiang, X. Wang, G. Wang, C. Hao, X. Li, T. Li, Adsorption performance of a polysaccharide composite hydrogel based on crosslinked glucan/chitosan for heavy metal ions, Composites, Part B, 169 (2019) 45–54.

[2] A. Mohammadi, P. Veisi, High adsorption performance of β-cyclodextrin-functionalized multi-walled carbon nanotubes for the removal of organic dyes from water and industrial wastewater, J. Environ. Chem. Eng., 6 (2018) 4634–4643.

[3] M.K. Uddin, A review on the adsorption of heavy metals by clay minerals, with special focus on the past decade, Chem. Eng. J., 308 (2017) 438–462.

[4] Y. Wu, H. Pang, Y. Liu, X. Wang, S. Yu, D. Fu, J. Chen, X. Wang, Environmental remediation of heavy metal ions by novel-nanomaterials: a review, Environ. Pollut., 246 (2019) 608–620.

[5] C. Cai, M. Zhao, Z. Yu, H. Rong, C. Zhang, Utilization of nanomaterials for in-situ remediation of heavy metal(loid) contaminated sediments: a review, Sci. Total Environ., 662 (2019) 205–217.

[6] Y. Zhu, X. Liu, Y. Hu, R. Wang, M. Chen, J. Wu, Y. Wang, S. Kang, Y. Sun, M. Zhu, Behavior, remediation effect and toxicity of nanomaterials in water environments, Environ. Res., 174 (2019) 54–60.

[7] M.E. Mahmoud, E.A. Saad, M.A. Soliman, M.S. Abdelwahab, Removal of radioactive cobalt/zinc and some heavy metals from water using diethylenetriamine/2-pyridinecarboxaldehyde supported on NZVI, Microchem. J., 145 (2019) 1102–1111.

[8] Z. Fan, Q. Zhang, B. Gao, M. Li, C. Liu, Y. Qiu, Removal of hexavalent chromium by biochar supported nZVI composite: batch and fixed-bed column evaluations, mechanisms, and secondary contamination prevention, Chemosphere, 217 (2019) 85–94.

[9] S. Wang, M. Zha, M. Zhou, Y.C. Li, J. Wang, B. Gao, S. Sato, K. Feng, W. Yin, A.D. Igalavithana, P. Oleszczuk, X. Wang, Y.S. Ok, Biochar-supported nZVI (nZVI/BC) for contaminant removal from soil and water: a critical review, J. Hazard. Mater., 373 (2019) 820–834.

[10] B. Wang, Z. Sun, Q. Sun, J. Wang, Z. Du, C. Li, X. Li, The preparation of bifunctional electrospun air filtration membranes by introducing attapulgite for the efficient capturing of ultrafine PMs and hazardous heavy metal ions, Environ. Pollut., 249 (2019) 851–859.

[11] H. Xu, Y. Zhang, Y. Chen, W. Tian, Z. Zhao, J. Tang, Polyaniline/ attapulgite supported nanoscale zero-valent iron for the rival removal of azo dyes in aqueous solution, Adsorpt. Sci. Technol., 37 (2019) 217–235.

[12] Y. Wang, A. Chen, M. Peng, D. Tan, X. Liu, C. Shang, S. Luo, L. Peng, Preparation and characterization of a fluorizated kaoline modified melamine sponge as an absorbent for efficient and rapid oil/water separation, J. Cleaner Prod., 217 (2019) 308–316.

[13] Y. Xie, Y. Yi, Y. Qin, L. Wang, G. Liu, Y. Wu, Z. Diao, T. Zhou, M. Xu, Perchlorate degradation in aqueous solution using chitosan-stabilized zero-valent iron nanoparticles, Sep. Purif. Technol., 171 (2016) 164–173.

[14] B. Zhang, N. Chen, C. Feng, Z. Zhang, Adsorption for phosphate by crosslinked/non-crosslinked-chitosan-Fe(III) complex sorbents: characteristic and mechanism, Chem. Eng. J., 353 (2018) 361–372.

[15] X. Jin, Z. Zhuang, B. Yu, Z. Chen, Z. Chen, Functional chitosan-stabilized nanoscale zero-valent iron used to remove acid fuchsine with the assistance of ultrasound, Carbohydr. Polym., 136 (2016) 1085–1090.

[16] N. Sun, Y. Zhang, L. Ma, S. Yu, J. Li, Preparation and characterization of chitosan/purified attapulgite composite for sharp adsorption of humic acid from aqueous solution at low temperature, J. Taiwan Inst. Chem. Eng., 78 (2017) 96–103.

[17] Y. Deng, L. Wang, X. Hu, B. Liu, Z. Wei, S. Yang, C. Sun, Highly efficient removal of tannic acid from aqueous solution by chitosan-coated attapulgite, Chem. Eng. J., 181–182 (2012) 300–306.

[18] R. Baghel, S. Upadhyaya, S.P. Chaurasia, K. Singh, S. Kalla, Optimization of process variables by the application of response surface methodology for naphthol blue black dye removal in vacuum membrane distillation, J. Cleaner Prod., 199 (2018) 900–915.

[19] A. Muthukkumaran, K. Aravamudan, Combined homogeneous surface diffusion model–design of experiments approach to optimize dye adsorption considering both equilibrium and kinetic aspects, J. Environ. Manage., 204 (2017) 424–435.

[20] H. Hu, Y. Wu, Z. Zhu, Optimization of microwave-assisted preparation of TPA from waste PET using response surface methodology, J. Polym. Environ., 26 (2018) 375–382.

[21] A. Sreedharan, S.T. Ong, Combination of Plackett–Burman and response surface methodology experimental design to optimize Malachite Green dye removal from aqueous environment, Chem. Data Collect., 25 (2020) 100317, doi: 10.1016/j.cdc.2019.100317.

[22] J. Zhou, X. Yu, C. Ding, Z. Wang, Q. Zhou, H. Pao, W. Cai, Optimization of phenol degradation by *Candida tropicalis* Z-04 using Plackett–Burman design and response surface methodology, J. Environ. Sci., 23 (2011) 22–30.

[23] D. Gao, Y. Zhang, B. Lyu, P. Wang, J. Ma, Nanocomposite based on poly (acrylic acid) / attapulgite towards flame retardant of cotton fabrics, Carbohydr. Polym., 206 (2019) 245–253.

[24] M. Gu, Q. Sui, U. Farooq, X. Zhang, Z. Qiu, S. Lyu, Degradation of phenanthrene in sulfate radical based oxidative environment by nZVI-PDA functionalized rGO catalyst, Chem. Eng. J., 354 (2018) 541–552.

[25] H. Li, Q. Zhou, F. Liu, W. Zhang, Z. Tan, H. Zhou, Z. Huang, S. Jiao, Y. Kuang, Biomimetic design of ultrathin edge-richedFeOOH@Carbon nanotubes as high-efficiency electro-catalysts for water splitting, Appl. Catal., B, 255 (2019) 117755, doi: 10.1016/j.apcatb.2019.117755.

[26] T. Wang, J. Su, X. Jin, Z. Chen, M. Megharaj, R. Naidu, Functional clay supported bimetallic nZVI/Pd nanoparticles used for removal of methyl orange from aqueous solution, J. Hazard. Mater., 262 (2013) 819–825.

[27] Y. Wu, Q. Yue, Z. Ren, B. Gao, Immobilization of nanoscale zero-valent iron particles (nZVI) with synthesized activated carbon for the adsorption and degradation of chloramphenicol (CAP), J. Mol. Liq., 262 (2018) 19–28.

[28] X. Li, L. Huang, H. Fang, G. He, D. Reible, C. Wang, Immobilization of phosphorus in sediments by nano zero-valent iron (nZVI) from the view of mineral composition, Sci. Total Environ., 694 (2019) 133695, doi: 10.1016/j.scitotenv.2019.133695.

[29] X.F. Zhao, Z.L. Liu, X.D. Li, S.P. Li, F.G. Song, The performance of attapulgite hybrids combined with MTX and Au nanoparticles, J. Phys. Chem. Solids, 124 (2019) 73–80.

[30] Y. Chen, W. Long, H. Xu, Efficient removal of Acid Red 18 from aqueous solution by in-situ polymerization of polypyrrole-chitosan composites, J. Mol. Liq., 287 (2019) 110888, doi: 10.1016/j.molliq.2019.110888.

[31] L. Chen, T. Yuan, R. Ni, Q. Yue, B. Gao, Multivariate optimization of ciprofloxacin removal by polyvinylpyrrolidone stabilized NZVI/Cu bimetallic particles, Chem. Eng. J., 365 (2019a) 183–192.

[32] D.M.K. Nguyen, T. Imai, T.L.T. Dang, A. Kanno, T. Higuchi, K. Yamamoto, M. Sekine, Response surface method for modeling the removal of carbon dioxide from a simulated gas using water adsorption enhanced with a liquid-film-forming device, J. Environ. Sci., 65 (2018) 116–126.

[33] G.D. Vyavahare, R.G. Gurav, P.P. Jadhav, R.R. Patil, C.B. Aware, J.P. Jadhav, Response surface methodology optimization for sorption of malachite green dye on sugarcane bagasse biochar and evaluating the residual dye for phyto and cytogenotoxicity, Chemosphere, 194 (2018) 306–315.

[34] U. Roy, S. Sengupta, P. Banerjee, P. Das, A. Bhowal, S. Datta, Assessment on the decolourization of textile dye (Reactive Yellow) using *Pseudomonas* sp. immobilized on fly ash: response surface methodology optimization and toxicity evaluation, J. Environ. Manage., 223 (2018) 185–195.

[35] P. Gharbani, Modeling and optimization of reactive yellow 145 dye removal process onto synthesized MnO_X-CeO_2 using response surface methodology, Colloid Surf., A, 548 (2018) 191–197.

[36] R. Subramaniam, S.K. Ponnusamy, Novel adsorbent from agricultural waste (cashew NUT shell) for methylene blue dye removal: optimization by response surface methodology, Water Resour. Ind., 11 (2015) 64–70.

[37] R.R. Madvaar, M.A. Taher, H. Fazelirad, Synthesis and characterization of magnetic halloysite-iron oxide nanocomposite and its application for naphthol green B removal, Appl. Clay Sci., 137 (2017) 101–106.

[38] S.E. Rizk, M.M. Hamed, Batch sorption of iron complex dye, naphthol green B, from wastewater on charcoal, kaolinite, and tafla, Desal. Water Treat., 56 (2015) 1536–1546.

[39] M.F. Attallah, I.M. Ahmed, M.M. Hamed, Treatment of industrial wastewater containing Congo Red and Naphthol Green B using low-cost adsorbent, Environ. Sci. Pollut. Res., 20 (2013) 1106–1116.

[40] Y. Chen, Z. Lin, R. Hao, H. Xu, C. Huang, Rapid adsorption and reductive degradation of Naphthol Green B from aqueous solution by Polypyrrole/Attapulgite composites supported nanoscale zero-valent iron, J. Hazard. Mater., 371 (2019b) 8–17.

[41] F. Zhang, Z. Ni, S. Xia, X. Liu, Q. Wang, Removal of Naphthol Green B from aqueous solution by calcined layered double hydroxides: adsorption property and mechanism studies, Chin. J. Chem., 27 (2009) 1767–1772.

[42] C. Lu, J. Yao, T.S. Knudsen, M. Made, J. Gu, J. Liu, H. Li, Z. Junyang, Degradation of a-nitroso-b-naphthol by UVA-B activated peroxide, persulfate and monopersulfate oxidants in water, J. Cleaner Prod., 238 (2019) 117942, doi: 10.1016/j.jclepro.2019.117942.

[43] J.S. Clemente, P.M. Fedorak, A review of the occurrence, analyses, toxicity, and biodegradation of naphthenic acids, Chemosphere, 60 (2005) 585–600.

[44] S. Cheng, N. Li, L. Jiang, Y. Li, B. Xu, W. Zhou, Biodegradation of metal complex Naphthol Green B and formation of iron–sulfur nanoparticles by marine bacterium *Pseudo alteromonas* sp CF10-13, Bioresour. Technol., 273 (2019) 49–55.